nature physics

Article

https://doi.org/10.1038/s41567-026-03292-6

Spatially anisotropic Kondo resonance coupled with the superconducting gap in a kagome metal

Received: 27 February 2025

Accepted: 14 April 2026

Published online: 15 May 2026

Check for updates

Zichen Huang[1,2,6], Hui Chen[1,2,3,6] ✉, Zhongqin Zhang[4,6], Hao Zhang[1,2,6], Zhen Zhao[1,2], Ruwen Wang[1,2], Haitao Yang[1,2,3], Wei Ji[4] ✉, Ziqiang Wang[5] & Hong-Jun Gao[1,2,3] ✉

The chromium-based kagome metal $CsCr_3Sb_5$ has garnered broad interest owing to its strong electron correlations, intertwined orders and potential for unconventional superconductivity under high pressure. The evolution of magnetic and superconducting interactions as the more frequently studied CsV_3Sb_5 is doped to $CsCr_3Sb_5$ remains poorly understood. Here we demonstrate the emergence of a spatially anisotropic Kondo resonance intertwined with the superconducting gap, enabled by introducing magnetic Cr impurities into the kagome superconductor CsV_3Sb_5. The addition of dilute Cr impurities not only weakens the long-range charge density wave order but also produces local magnetic moments, which leads to Kondo resonances. We show that the Kondo resonance forms anisotropic, ripple-like spatial patterns around individual Cr atoms, breaking all local mirror symmetries. We further reveal that, with the emergence of Kondo screening, the coherence peak and depth of the superconducting gap with finite zero-energy conductance are enhanced. This suggests that non-superconducting carriers at the Fermi surface in the parent compound participate in the Kondo effect, simultaneously screening Cr magnetic moments and increasing the superfluid density. Our findings offer an opportunity to study the interplay between superconductivity and local magnetism in kagome materials.

The interplay between magnetism and superconductivity has been a central topic in condensed matter physics. Although magnetism generally suppresses phonon-mediated conventional superconductors, magnetic fluctuations are widely considered to be a key pairing mechanism in unconventional superconductors (USCs). Antiferromagnetic (AFM) fluctuations are the most common driving force of superconductivity in cuprates, iron-based superconductors and heavy-fermion superconductors[1,2], whereas ferromagnetic fluctuations have been associated with spin-triplet superconductivity, for example, in UTe_2 (ref. 3). Recently, the vanadium-based kagome metals AV_3Sb_5 (A = K, Rb or Cs) have drawn sustained interest as kagome systems exhibiting superconductivity[4,5]. AV_3Sb_5 compounds possess a cascade of exotic phenomena such as multiple Van Hove singularities near the Fermi level[6,7], nontrivial Z_2 topology[5], an anomalous Hall effect[8], pair density waves[9–11] and electronic nematicity[12–14]. AV_3Sb_5 has a V-shaped superconducting (SC) gap with sign-preserving multi-band

[1]Beijing National Center for Condensed Matter Physics and Institute of Physics, Chinese Academy of Sciences, Beijing, People's Republic of China. [2]School of Physical Sciences, University of Chinese Academy of Sciences, Beijing, People's Republic of China. [3]Hefei National Laboratory, Hefei, People's Republic of China. [4]Beijing Key Laboratory of Optoelectronic Functional Materials and Micro-Nano Devices, School of Physics, Renmin University of China, Beijing, People's Republic of China. [5]Department of Physics, Boston College, Chestnut Hill, MA, USA. [6]These authors contributed equally: Zichen Huang, Hui Chen, Zhongqin Zhang, Hao Zhang. ✉e-mail: hchenn04@iphy.ac.cn; wji@ruc.edu.cn; hjgao@iphy.ac.cn

superconductivity[15,16], and the superconductivity in this class of material has been proved to be sensitive to external perturbation. Double-dome superconductivity and unconventional competition with charge density waves (CDWs) are observed under pressure[17,18]. In addition, chemical substitution provides an additional tuning parameter, yielding complex phase diagrams with intertwined instabilities, such as hole doping via Ti substitution[19,20] and isovalent substitution with Ta or Nb[21,22]. However, the doping-induced magnetism in kagome superconductors has rarely been explored.

Substituting V with magnetic Cr is expected to introduce magnetism into CsV_3Sb_5 (refs. 23–25). In addition, the related chromium-based material $CsCr_3Sb_5$ shares the same crystal structure and exhibits an AFM transition below 55 K at ambient pressure. With increasing pressure, the AFM order is suppressed and superconductivity emerges at 4.2 GPa, near the quantum criticality point[26,27]. The multi-phase diagram of $CsCr_3Sb_5$ resembles that of other USCs, and AFM fluctuations have been proposed as the pairing mechanism, positioning $CsCr_3Sb_5$ as a potential USC candidate within kagome systems. Clarifying how Cr doping modifies the magnetism and superconductivity in CsV_3Sb_5 is therefore essential for understanding both the AFM order and pressure-induced superconductivity in kagome systems.

Here, we investigate the interaction between local magnetic moments and superconductivity in the magnetic Cr-doped kagome superconductor $CsV_{3-x}Cr_xSb_5$ by utilizing ultralow temperature scanning tunnelling microscopy/spectroscopy (STM/STS). In addition to the gradual suppression of the long-range CDW order, dilute Cr doping induces Kondo resonances near the Fermi level, arising from the screening of local magnetic moments. The resonances propagate preferentially along one of the four equivalent directions, thereby breaking all local mirror symmetries. Density functional theory (DFT) calculations reveal that the V–Cr AFM coupling induces magnetic frustration among V sites in the V–Sb kagome layer near Cr dopants, leading to ripple-like propagation of spin density, which contributes to the observed anisotropic Kondo resonance. Simultaneously, superconductivity evolves noticeably with Cr doping. In the Kondo resonance phase, the coherence peak height and gap depth of the SC gap markedly enhance, accompanied by an unconventional spatial evolution of vortex-bound states (VBS). Once the Kondo resonance disappears, the superconductivity is rapidly suppressed by magnetic ordering. These findings reveal a distinct SC phase in $CsV_{3-x}Cr_xSb_5$, providing insight into the coupling between superconductivity and magnetism in kagome metals.

We first investigate the topographic characteristics of Cr dopants in CsV_3Sb_5, achieved by substituting V atoms with Cr in the V–Sb kagome plane. The concentration of Cr dopants is described by x in the $CsV_{3-x}Cr_xSb_5$ (Fig. 1a). We have synthesized a series of $CsV_{3-x}Cr_xSb_5$ with x ranging from 0 to 1.2 (Fig. 1b–g and Supplementary Fig. 1). Compared with a pristine sample, there are additional dumbbell-like topographic protrusions in the STM images of Sb-terminated surfaces (Fig. 1h). The density of the dumbbell-like protrusions increases simultaneously with the Cr concentrations (Fig. 1b–g). We thus attribute the dumbbell-like protrusions to the Cr dopants. The Cr dopants are embedded in the middle of two adjacent topmost Sb atoms, which results in two-fold dumbbell-like protrusions located halfway between pairs of topmost Sb atoms (Fig. 1h). There are three equivalent two-fold axes of dumbbell-like protrusions, which correlates to three lattice directions (Fig. 1a, green shades).

We then study the evolution of CDW orders with the Cr concentration by performing the Fourier transform (FT) of topographic images. In pristine CsV_3Sb_5, the long-range 2×2 CDW ($\mathbf{Q}_{3q\text{-}2a}$) and $4a_0$ unidirectional charge order ($\mathbf{Q}_{1q\text{-}4a}$) have been observed at the Sb surfaces[9,28]. For the dilute doped sample ($x = 0.012$), the Bragg peaks together with a clear signature of $\mathbf{Q}_{3q\text{-}2a}$ and $\mathbf{Q}_{1q\text{-}4a}$ are observed (Fig. 1i). For the $x = 0.3$ sample, the intensity of the CDW peaks become much weaker (Supplementary Fig. 1a–f). Thus, we plot the fast Fourier transform profile along the high symmetry direction of samples, which shows that the peak intensity of both $\mathbf{Q}_{3q\text{-}2a}$ and $\mathbf{Q}_{1q\text{-}4a}$ gradually reduces with increasing Cr concentration (Fig. 1j). The CDWs are nearly undetectable at a large concentration of $x = 1.2$, consistent with transport results showing complete suppression of the CDW transition at $x = 0.36$ (refs. 23–25) (Supplementary Fig. 1g).

Apart from the suppression of long-range charge orders, the dilute magnetic Cr dopants also introduce local magnetic moments. The local moments are screened by the surrounding itinerant electrons from the non-magnetic metallic band of CsV_3Sb_5, which results in the Kondo resonance in the density of state[29,30]. The Kondo resonance exhibits a pronounced peak with an asymmetric spectral shape near the Fermi level in the representative dI/dV spectra obtained upon the Cr dopants of Cr-doped CsV_3Sb_5 (that is, $x = 0.03$; Fig. 2a). We define the energy corresponding to the maximum intensity of this resonance system with local electron–hole asymmetry as the Kondo resonance position, P_{kondo}. Such a peak is absent from the dI/dV spectra of the dopant-free region. Except for the Kondo resonance peak at $P_{kondo} \approx -3$ meV, as shown in Fig. 2a, there are no magnetic impurity states inside the SC gap, which indicates that the Cr-doped sample reaches the strong coupling regime owing to the Kondo screening of the impurity magnetic moment[31].

We note that P_{kondo} could vary from −5 meV to 5 meV for different Cr dopants at the Sb surface of a Cr-doped sample (Supplementary Fig. 2). The energy range of P_{kondo} falls well within the range reported in earlier works[32,33]. This variation probably arises from spatial inhomogeneity in the surface electronic states introduced by Cr doping, which modifies the local electronic environment of each magnetic impurity and shifts the Kondo resonance position. The P_{kondo} variations become more pronounced at higher Cr concentrations (Supplementary Fig. 2) with enhanced inhomogeneity of surface states, further supporting this interpretation.

To advance our understandings on the Kondo resonance, the typical dI/dV spectrum was fitted to the Frota function[34,35]. The half width at half maximum (HWHM) of the Kondo peak width fitted by the Frota function is determined to be about 1.43 mV (Fig. 2b). On the basis of the fitting of the dI/dV spectrum obtained at ultralow temperature (5 mK) and the function $T_K = \Gamma_{HWHM}/3.92k_B$, the Kondo temperature is estimated to be approximately 4.23 ± 0.13 K. The evolution of the dI/dV spectra with an external magnetic field perpendicular to the sample surface (B_z) shows the splitting of the Kondo peak. With increasing B_z, the resonance peak first stays mostly unchanged. When $B_z > 5$ T, the single resonance peak starts to split into two peaks at the positions of P_+ and P_- (Fig. 2c). Such evolution is clearer in the second derivative of the dI/dV spectra (Fig. 2d). The linear splitting of the resonance peak corresponds to the Zeeman splitting of the spin doublet for the local moment of the Cr dopant. We describe the two split peaks using double Frota functions (Supplementary Fig. 3) and obtain the linear relationship between the splitting energy $\Delta_{split} = P_+ - P_-$ and the magnetic field B_z as $\Delta_{split} = 0.93\mu_B|B_z|$ (Fig. 2e). The moment estimated from the linear fitting ($0.93\,\mu_B$) is close to the effective magnetic moment $\mu_{eff} = 1.26 \pm 0.12\,\mu_B$ per Cr atom[26]. An intuitive explanation is that the spin orientation of the local moment around the Cr dopant is parallel to the kagome plane and a strong out-of-plane magnetic field flops the spin from an in-plane to out-of-plane direction, leading to the Zeeman splitting. Such phenomena are in agreement with the Kondo effect in the strong coupling regime[36,37].

To estimate the characteristic temperature scale of the Kondo resonance, we also study the temperature evolution of the dI/dV spectra for the same Cr dopant. As the temperature increases from 6 K to 12 K, the resonance peak broadens rapidly with increasing temperature (Fig. 2f, green dots). To extract the temperature evolution of the Kondo resonance, we apply the Frota model, taking the Fermi–Dirac broadening into consideration, that is, the Hurwitz–Fano lineshape[38], to fit the spectra at each temperature (Fig. 2g). We analyse the temperature broadening of the linewidth by employing the empirical expressions

https://doi.org/10.1038/s41567-026-03292-6

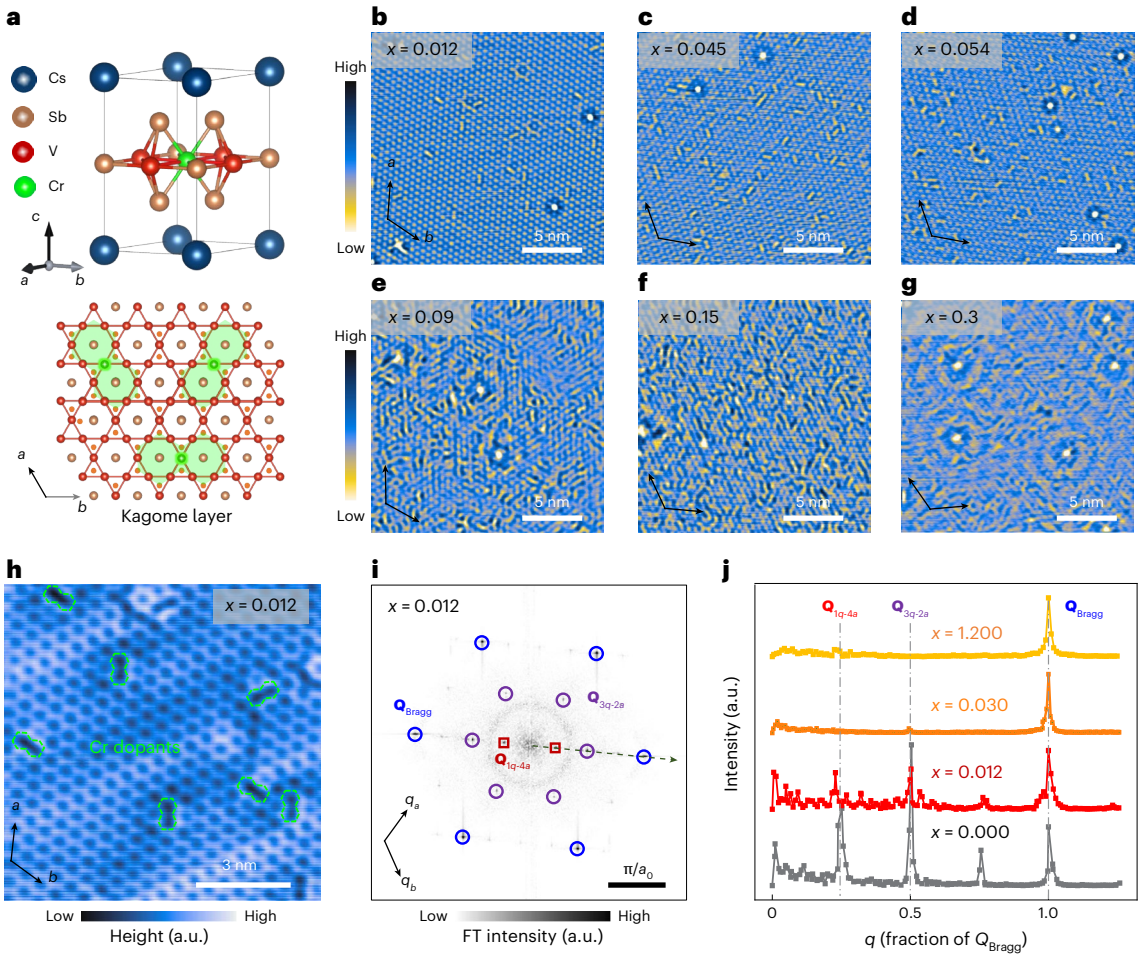

Fig. 1 | Atomic structures of $CsV_{3-x}Cr_xSb_5$ and evolution of CDWs with the Cr concentration. a, Top: an illustration of the $CsV_{3-x}Cr_xSb_5$ crystalline structure. $CsV_{3-x}Cr_xSb_5$ crystallizes in the parent CsV_3Sb_5 structure. Bottom: the Cr atoms substitute V atoms in the VSb kagome plane. **b**–**g**, STM images of Sb-terminated surface with different Cr concentrations x: 0.012 (**b**), 0.045 (**c**), 0.054 (**d**), 0.09 (**e**), 0.15 (**f**) and 0.3 (**g**), obtained at a base temperature of 5 mK. **h**, An atomically resolved STM image of the Sb surface with a Cr concentration x of 0.012, showing that Cr substitutions appear as twofold protrusions marked by green dumbbells ($V_s = 500$ mV, $I_t = 1$ nA). **i**, The Fourier transform (FT) of STM topography with $x = 0.012$. The Bragg peaks $\mathbf{Q}_{Bragg}$ are marked by blue circles. The vectors of 2×2 CDW, $\mathbf{Q}_{3q\text{-}2a}$, and $4a_0$ unidirectional charge order, $\mathbf{Q}_{1q\text{-}4a}$, are marked by purple circles and red squares, respectively ($V_s = 100$ mV, $I_t = 0.1$ nA). **j**, The evolution of the FT profile along the high symmetry direction (dark-green arrow in **i**) with the Cr concentration x. The peak near $q = 0.75$ at $x = 0$ results from the satellite peak of $\mathbf{Q}_{1q\text{-}4a}$: $\mathbf{Q}'_{1Q\text{-}4a} = \mathbf{Q}_{Bragg} - \mathbf{Q}_{1Q\text{-}4a}$ (ref. 28). The bias of the topography for the FT is $V_s = -100$ mV.

$\Gamma_{HWHM} = \sqrt{(\alpha k_B T)^2 + 2(k_B T_{K,N})^2}$, yielding the parameter values of $T_{K,N} = 11.5 \pm 0.2$ K and $\alpha = 2.10 \pm 0.03$, where $T_{K,N}$ denotes the Kondo temperature parameter defined in ref. 38. The Kondo temperature is estimated to be $T_K = T_{K,N}/2.77 = 4.15 \pm 0.09$ K, comparable to the value of ~4.23 K estimated by the ultralow temperature single spectrum fitting in Fig. 2b.

It is worth noting that the temperature evolution is not sufficiently described by the recently derived expression that was successfully applied in a spin-1/2 Kondo impurity studied in single molecule works[38] as the correlated states in our system may involve other spin interactions that are insufficiently captured by the model for a $S = 1/2$ single magnetic molecule on a metallic substrate. Alternative origins for impurity-induced electronic states near the Fermi level, beyond the Kondo scenario, can be excluded. The spinaron scenario would yield multiple field-sensitive features rather than a single Zeeman-split peak[39], and orbital excitations would produce symmetric step-like inelastic tunnelling features[40], none of which are observed.

We next study the real-space distribution of the Cr dopant-induced Kondo resonance. In contrast to the symmetric real-space distribution of the Kondo resonance in previous reports[41,42], the spatial distribution of the Kondo resonance shows symmetry-breaking ripple-like patterns surrounding the Cr dopant. In the STM topographic image obtained on the Sb surface of the $x = 0.012$ sample at large sample bias, that is, 500 mV, the Cr dopants appear as symmetric two-fold dumbbells (Figs. 1h and 3a). The dI/dV spectrum of the dopant shown in Fig. 3a exhibits a Kondo peak at +5 mV (different from Fig. 2a, as peak energies vary from dopant to dopant; Supplementary Fig. 2). When the sample bias is set at around the Kondo peak (that is, 10 mV in Fig. 3b; see Supplementary Fig. 4 for details), bright 'ripples' propagating along one of the lattice directions appear around the dopant (Fig. 3b). The distance between each protrusion in the ripple equals the lattice constant a_0.

The bright protrusions are located within the V-formed triangles in the kagome structure, and the Cr dopant is embedded in the spatial location between the first two bright protrusions. The spatial distribution of the Kondo resonance is further demonstrated by the dI/dV linecut (Fig. 3c) along the stripe direction and a direction rotated by 120°, respectively. In addition, the dI/dV map at 5 meV (Fig. 3d), which corresponds to P_{kondo}, exhibits similar symmetry-breaking ripples to the low-energy STM image. By contrast, the dI/dV map obtained at an energy away from the Kondo resonance, that is, −5 meV, shows an opposite feature to that at 5 meV, with a stripe pattern formed by a

https://doi.org/10.1038/s41567-026-03292-6

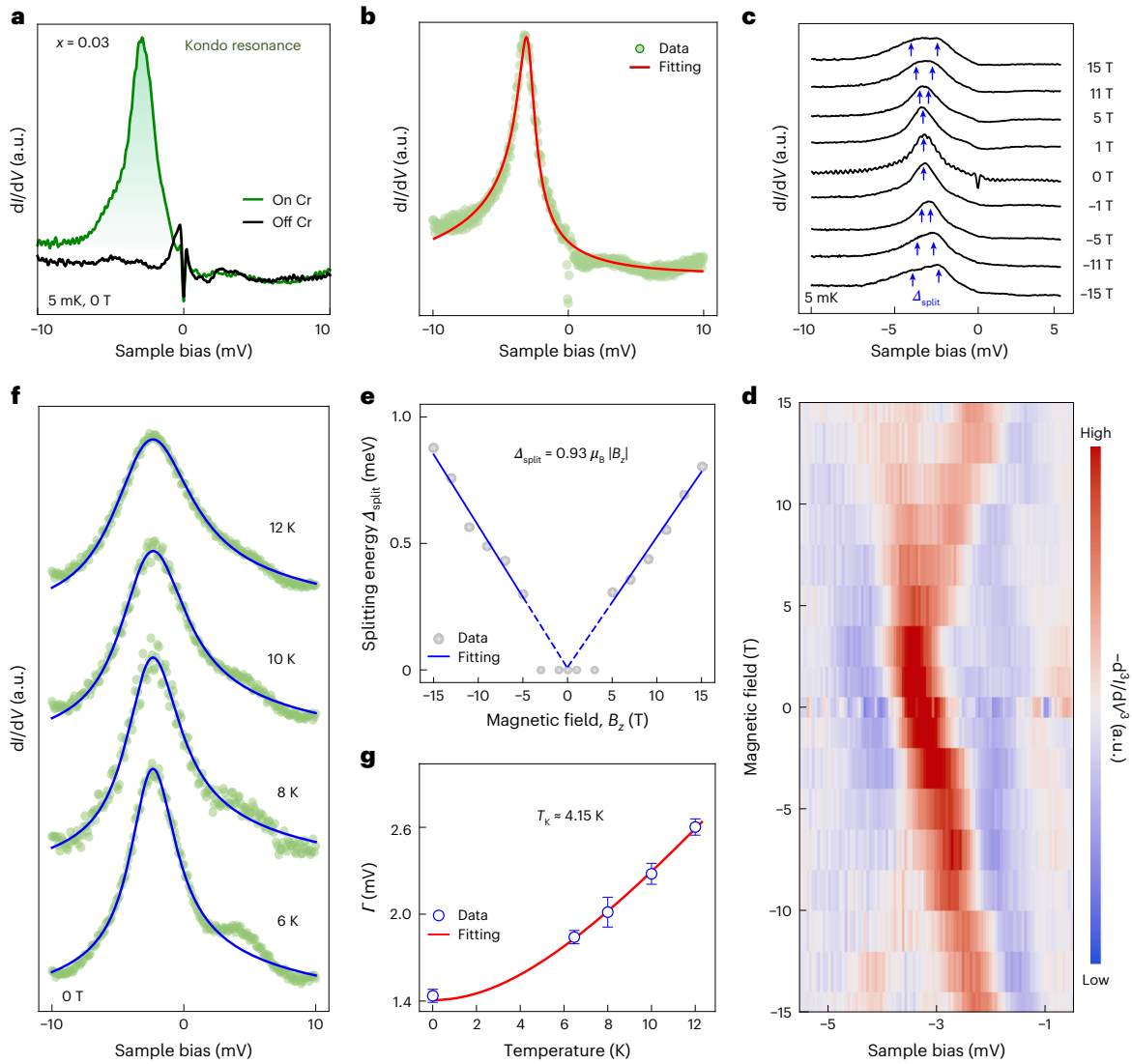

Fig. 2 | Field and temperature evolution of the Kondo resonance on the Cr dopants of $CsV_{3-x}Cr_xSb_5$ (x = 0.03). **a**, dI/dV spectra taken away from the Cr dopant (black) and on the Cr dopant (green) (V_s = 10 mV, I_t = 1 nA, V_{mod} = 50 μV, T_{base} = 5 mK), showing a pronounced Kondo resonance peak on the Cr dopant. **b**, The dI/dV spectra at the Cr dopant (green dots), showing that the Kondo peak can be fitted by a Frota function (red curve), with an HWHM of ~1.43 mV. **c**,**d**, The magnetic field evolution of the dI/dV spectra (**c**) and the second-derivative curves (**d**) on Cr dopants, showing Zeeman splitting of the Kondo peak at fields above 5 T (V_s = 10 mV, I_t = 1 nA, V_{mod} = 50 μV, T_{base} = 5 mK). **e**, The magnetic field dependence of the splitting Δ (grey dots) with a linear fit (blue line), yielding the relation $\Delta_{split} = 0.93\,\mu_B|B_z|$. Δ shows no sign of splitting with $B < 5$ T and is therefore set to 0. **f**, The temperature dependence of dI/dV spectra, showing the gradual broadening of the Kondo peak with increasing temperature. Blue curves represent the fitting results with the Frota model, taking the Fermi–Dirac broadening into consideration (Hurwitz–Fano lineshape[38]) (V_s = −10 mV, I_t = 1 nA, V_{mod} = 50 μV). **g**, The HWHM of the Kondo peak as a function of temperature. The HWHMs are retrieved from the fittings in **f**. The relationship between them is fitted using the empirical expression, which gives $\alpha = 2.1$ and $T_K \approx 4.15 \pm 0.09$ K. Error bars in **g** represent the deviations from the Frota fitting.

reduction of the local density of states (LDOS) (Fig. 3e). These observations demonstrate that the anisotropic stripe patterns are a characteristic spatial distribution of the Kondo resonance. Such an anisotropic Kondo resonance is universal with respect to different Cr dopants (the same spectroscopic measurement for adjacent Cr dopant is shown in Supplementary Fig. 5). The anisotropic real-space distribution of the Kondo resonance is observed on samples with different Cr concentrations, despite the variations in P_{kondo} (Supplementary Fig. 6). The ripple direction is randomly aligned with one of the four equal lattice directions (Supplementary Fig. 7).

External strain can be ruled out as the origin of this directionality. Strain from the substrate or mounting would be non-uniform and sensitive to cleaving or mounting conditions, yet the observed directionality is reproducible in the spectra obtained at single Cr dopants across eight samples prepared under varied conditions. Moreover, uniaxial strain in kagome metals is known to produce surface-corrugated regions[43], which are absent from our measurements. Finally, strain-induced anisotropy should lead to distinct strain domains, whereas the ripple directions that we observe are randomly aligned along one of the four equivalent lattice axes.

The observed anisotropic Kondo resonance state may originate from either the Kondo screening process or the spatial distribution of Cr dopant-induced magnetic moments. Given the kagome-latticed V–Sb layer, where competing interactions induce magnetic frustration, the anisotropic spatial distribution of magnetic moments is the more plausible explanation. By contrast, the delocalized nature of conduction electrons typically favours isotropic screening. Our DFT calculations verify the anisotropic distribution of induced magnetic moments. The kagome-latticed V–Sb layer undergoes a CDW phase transition, where V atoms form alternating triangular and hexagonal

https://doi.org/10.1038/s41567-026-03292-6

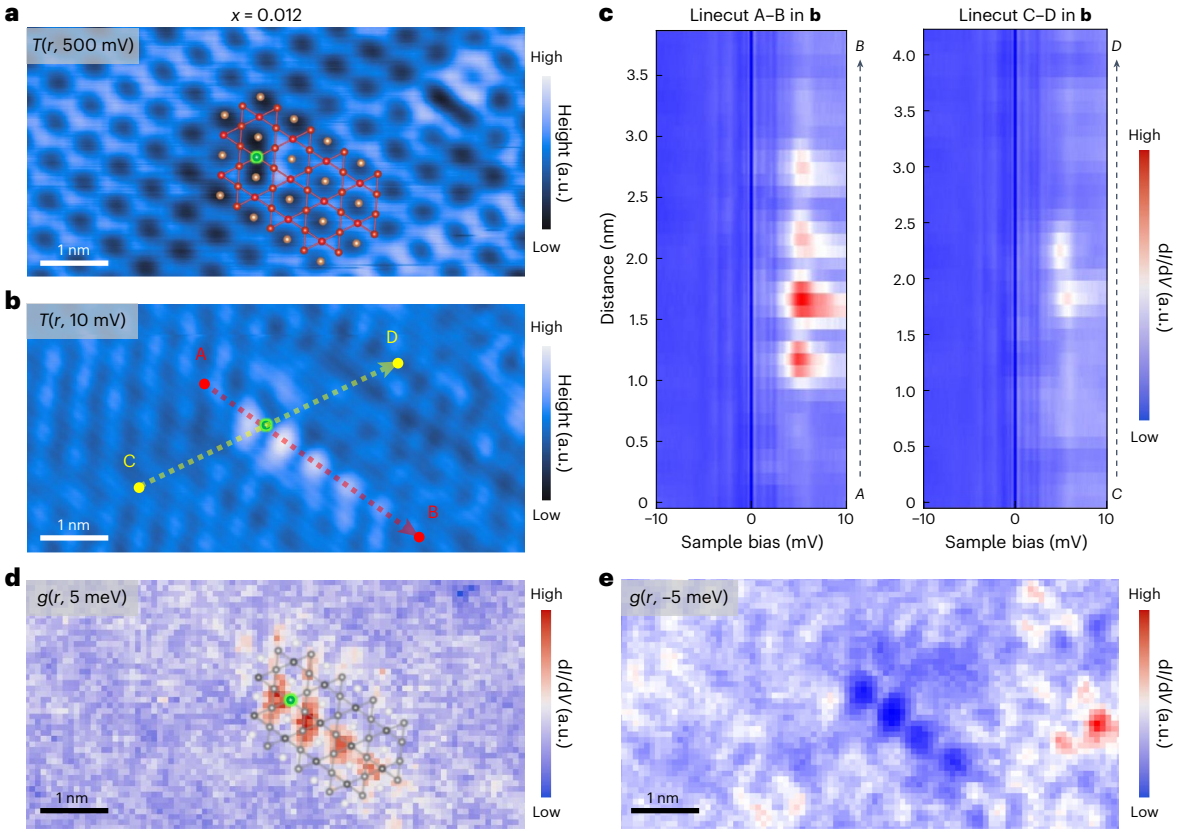

Fig. 3 | The anisotropic distribution of the Kondo resonance in real space. **a**,**b**, A comparison of an STM image of the same area with a scanning bias of 500 mV (**a**) and 10 mV (**b**) for the sample with $x = 0.012$. A schematic model is overlaid in **a**, showing that the direction of the bright protrusions in **b** is along a lattice direction. The distance between each protrusion equals the lattice constant a_0. **c**, A colour plot of the dI/dV linecut across a Cr dopant in directions parallel to the a axis (red arrow from position A to B in **b**) and at 60° to the a axis (yellow arrow from position C to D in **b**) ($V_s = 10$ mV, $I_t = 1$ nA, $V_{mod} = 50$ μV, $T_{base} = 5$ mK). **d**,**e**, The LDOS map at 5 meV (**d**) and −5 meV (**e**).

arrangements that exhibit a slightly different preference for Cr substitution. Specifically, Cr substitution at a hexagonal V site is energetically favoured over substitution at a triangular site, by 1.6 meV per Cr. The fully relaxed atomic structure of the V–Sb layer with a Cr dopant replacing a hexagonal V atom is shown in Fig. 4a and Supplementary Fig. 8a,b. The simulated STM image shown in Supplementary Fig. 8c agrees with the experimental images. The presence of CDW-induced structural distortion breaks the mirror symmetry M_y, which passes through the Cr atom and is parallel to the y–z plane. We emphasize that the 1Q charge order is not considered in the calculations because it is not correlated with the observed unidirectionality of the Kondo resonance (Supplementary Fig. 7) and is probably of surface origin[44]. Furthermore, Cr substitution introduces in-plane compressive strain, leading to asymmetric Cr–V bond lengths (Fig. 4b), which, in turn, lifts an additional mirror symmetry M_x where the x–z plane serves as the mirror plane. In addition, the comparable lengths of these four Cr–V bonds imply that the Cr dopant can suppress the CDW order, which is consistent with experimental observations where the CDW signal disappears with an increase in the Cr concentration (Fig. 1j).

The Cr dopant has one more d electron than an adjacent V atom, thereby introducing a local magnetic moment of 1.98 μ_B per Cr, surrounded by non-local electrons from neighbouring surface V atoms. Owing to the magnetic proximity effect, the Cr local moment magnetizes adjacent V atoms through AFM couplings. Such Cr dopant-induced local magnetization leads to strong spin frustration within the kagome V–Sb layer (Fig. 4c). This frustration gives rise to at least four candidate magnetic configurations (Supplementary Fig. 8d–g), each of which contains four AFM and two ferromagnetic nearest-neighbour spin-exchange couplings within the corner-sharing bi-triangle unit show in Fig. 4c.

Our DFT calculations reveal that the magnetic configuration shown in Fig. 4d (V–Sb layer) is the most stable among these configurations. Regardless of the initial magnetic configuration chosen from those shown in Supplementary Fig. 8d–g, the system invariably relaxes to the magnetic configuration illustrated in Fig. 4d, where one of the four nearest-neighbouring V sites is polarized in alignment with the majority spin orientation (spin-up, red) of the Cr dopant. The spin-up V and the Cr dopant form a line-like feature in the spin-up density, which extends along the Cr–V direction with gradually diminishing intensity, resulting in a quasi-one-dimensional ripple-like propagation pattern through the lattice (Supplementary Fig. 8h). This spin density distribution in the Cr–V plane induces an anisotropic spin distribution on the Sb surface, as depicted in Fig. 4e and Supplementary Fig. 8i. These anisotropically distributed spin-up electrons undergo AFM coupling with itinerant electrons at low temperature, leading to the anisotropic Kondo resonance observed in our experiments. The theoretically predicted spatial distribution of spin-up charge density (Fig. 4e, pink isosurface contour superposing) at the Sb layer is comparable to the contour of the experimentally observed Kondo cloud in the dI/dV mapping acquired near the Fermi level (Fig. 4e, dotted blue contour). According to our calculations shown in Supplementary Fig. 9, the ferromagnetic coupled Cr–V bond consistently shows a moderate length (approximately 2.80 Å) among all four, indicating the Cr–V structure locking with spin-exchange interactions rather than 3Q-CDW-induced structural variations. The CDW order is further suppressed by Cr doping, and the direction of ferromagnetic coupled Cr–V bonds, and thus

https://doi.org/10.1038/s41567-026-03292-6

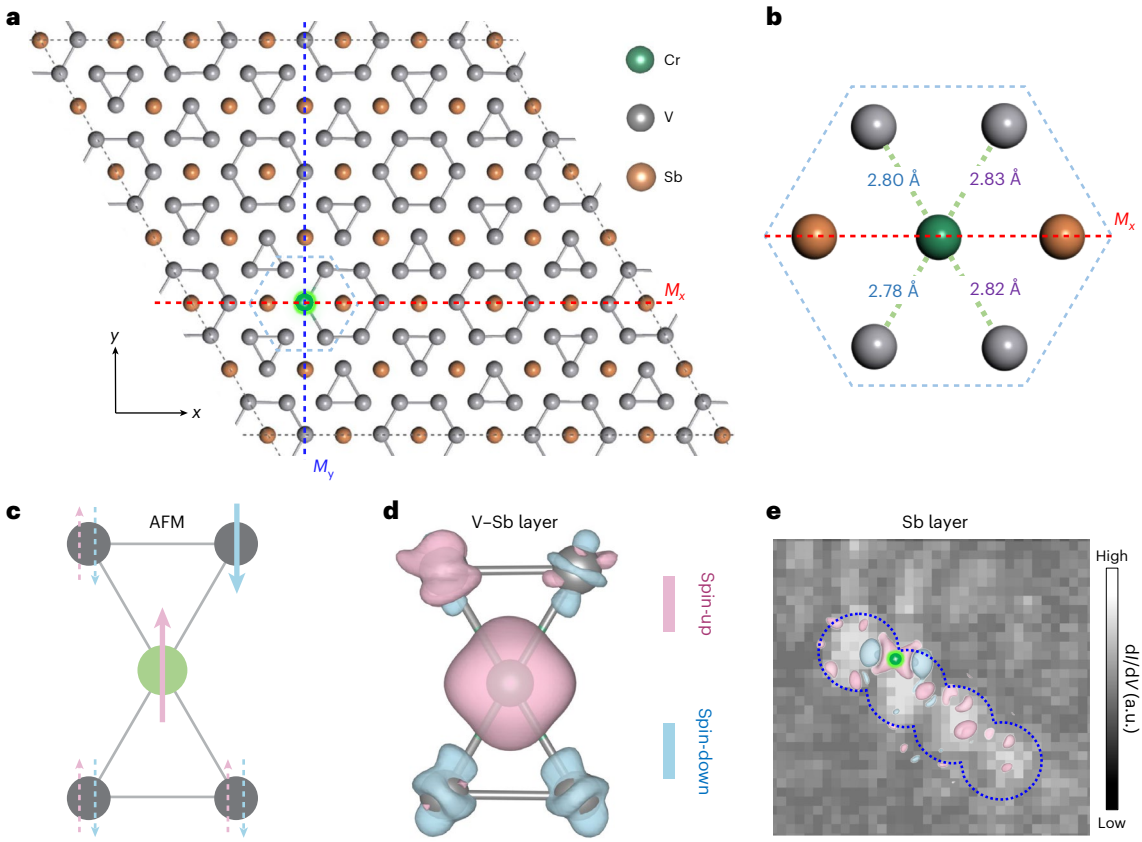

Fig. 4 | DFT calculations of the spin-density distribution around a Cr dopant in CsV_3Sb_5. a, A fully relaxed atomic structure model of the V–Sb kagome layer after a V atom is substituted by a Cr atom (highlighted by the green shade). **b**, A zoom-in of the dashed blue region in **a**. The dashed green lines indicate Cr–V bonds, with bond lengths labelled. The dashed blue and orange lines in **a** and **b** represent the mirror planes for mirror symmetry operations M_x and M_y, respectively. If the system has M_x symmetry, two blue (or purple) bond lengths in **b** should be equal. **c**, A schematic of the spin frustration in a di-triangle within a kagome lattice where the nearest-neighbouring sites are coupled antiferromagnetically. The green (black) circle(s) denote the site(s) of the Cr dopant (adjacent V atoms). The violet up and cyan down arrows indicate up and down spins, respectively. The pairs of up and down dashed arrows indicate that the spin is undetermined at this site owing to spin frustration. **d**, Isosurface contours of the spin densities of Cr and its four neighbouring V atoms for the most energetically favoured magnet configuration as revealed by DFT. The colour coding follows the same scheme used in **c** (violet for spin-up, cyan for spin-down). An isosurface value of 2×10^{-3} e bohr^{-3} was used for plotting. **e**, An experimental dI/dV mapping image acquired near a Cr dopant at a bias voltage of 5 mV (black and white image), decorated with the theoretical spin density at the Sb layer nearby a Cr atom of the magnetic configuration presented in **d**, using the same colour scheme as in **c** and **d**, and an isosurface value of 1.5×10^{-4} e bohr^{-3}. The bright green spot represents the Cr atom, whereas the dotted blue contour outlines the distribution of the spin-up charge density and the Kondo cloud.

the Kondo resonance direction, is not necessarily related to the initial 3Q-CDW structure. On the basis of such a model, shifting the Cr position step by step along the hexagonal 3Q-CDW bond is expected to rotate the Kondo-screening direction by 60° each time. This sixfold sequence of orientations is indeed observed in STM images (Supplementary Fig. 10).

The Kondo resonances are observed in all slightly doped sample (Supplementary Fig. 2). With increasing concentrations x of Cr, the resonance peak of the representative Kondo resonance gradually becomes broader and lower (Fig. 5a). It is worth noting that the peak positions of the Kondo resonance in Fig. 5a differ from those in Figs. 2 and 3, as the dI/dV spectra were measured on different Cr dopants (Supplementary Fig. 2). When x increases to 0.09, the Kondo resonance is indistinguishable in the low-energy dI/dV spectra (Supplementary Fig. 11). The suppression of the Kondo effect with increasing Cr concentrations may arise from enhanced Ruderman–Kittel–Kasuya–Yosida interactions between Cr dopants, which can lead to spin-glass-like behaviour and modify the Kondo response through impurity–impurity spin interactions[42,45], as suggested in fully substituted Cr–V kagome systems[46]. However, additional mechanisms may also contribute, and further studies are needed to clarify the underlying origin.

Meanwhile, the superconductivity shows an intriguing evolution with the Cr concentration, as indicated by the spatially averaged dI/dV spectra at a low temperature of 5 mK (Fig. 5b). In the pristine sample, the SC gap shows a V-shaped pairing gap with residual in-gap states[12]. In the slightly doped sample, the peak-to-peak SC gap size Δ_{SC} does not markedly change. However, the coherence peak height at the gap edge P_{SC} = dI/dV ($E = \Delta_{SC}$) and SC gap depth $H_{SC} = P_{SC}$ − dI/dV(E = 0) show different evolution with x. Both P_{SC} and H_{SC} become higher with increasing x and reach a maximum at x = 0.012.

The enhanced coherence peak and SC gap depth indicate higher superfluid density[47]. To further characterize the exotic superconductivity with enhanced gap depth, we apply vertical magnetic fields to the samples with x = 0.007 and 0.021 to investigate possible differences in Abrikosov vortices. By applying a 20 mT magnetic field, a hexagonal vortex lattice forms in both samples (Supplementary Fig. 12). However, the dI/dV linecut measured across the vortex and the corresponding second-derivative d^3I/dV^3 spectra showed different characteristics for these two different samples. For x = 0.007, an X-shaped spatial evolution of the VBS is observed (Fig. 5c), consistent with well-studied pristine CsV_3Sb_5. For x = 0.021, a non-splitting Y-shaped spatial evolution of the VBS is observed (Fig. 5c), different from pristine CsV_3Sb_5 and

https://doi.org/10.1038/s41567-026-03292-6

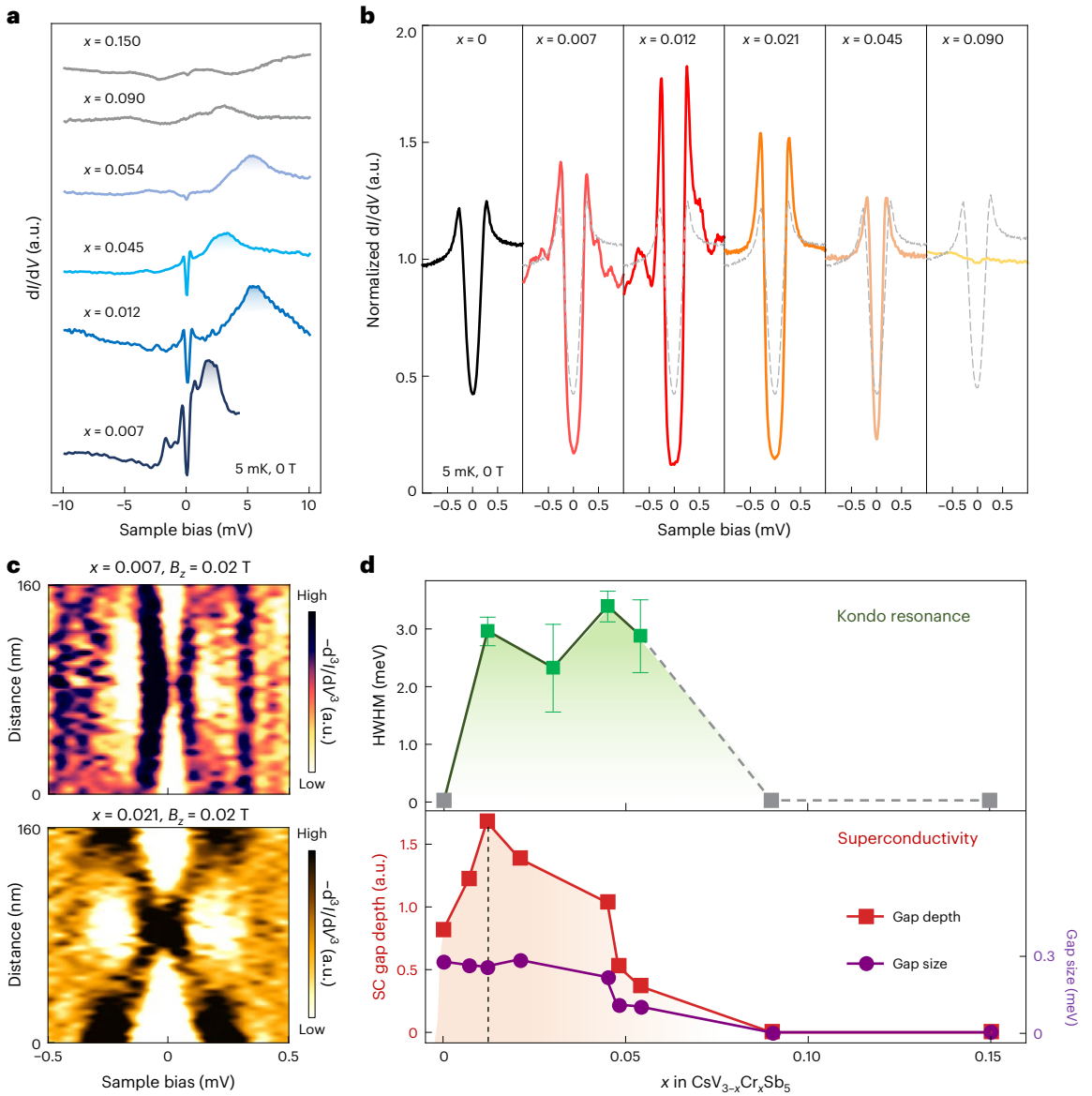

Fig. 5 | Intertwining Kondo resonance with superconductivity in $CsV_{3-x}Cr_xSb_5$. **a**, Representative d*I*/d*V* spectra of the Kondo resonance with Cr concentration *x* of 0.007, 0.012, 0.045, 0.054, 0.090 and 0.150, respectively. **b**, The evolution of the spatially averaged d*I*/d*V* spectra with different Cr concentrations ($V_s = -5$ mV, $I_t = 1$ nA, $V_{mod} = 10$ μV, $T_{base} = 5$ mK). **c**, The second derivative of the d*I*/d*V* linecut across the vortex core in the samples with $x = 0.007$ and $x = 0.021$, showing distinct spatial evolution of the VBS. **d**, The evolution of the Kondo resonance peak HWHM (top) and SC gap depth (left axis) and gap size (right axis) (bottom) with the Cr concentration *x*, showing strong coupling between the Kondo screening and superconductivity. The HWHM of the Kondo resonance at each concentration as determined by using the same Frota fitting procedure as in Fig. 2b and applied to multiple dopants at each concentration. The error bar represents the standard difference of the average HWHM in the fitting of the Kondo resonance for each concentration.

$CsV_{3-x}Cr_xSb_5$ with $x = 0.007$. Although trivial vortices typically exhibit an X-shaped evolution of the VBS, previous studies on a $Bi_2Te_3/NbSe_2$ heterostructure and 2M-WS_2 identified a non-splitting Y-shaped evolution as a signature of Majorana zero modes[48,49]. The change of the VBS behaviour when increasing the Cr concentration from 0 to 0.021 can be regarded as a possible modification of the topological surface band in the SC state[50], further supporting the existence of a distinct phase[51].

The phase diagram of the Kondo effect and the superconductivity versus Cr concentration shows the strong interplay of the superconductivity with the Kondo resonance (Fig. 5d). We use the HWHM of the Kondo peaks, extracted using the same Frota fitting procedure as in Fig. 2b and applied to multiple dopants at each concentration (Fig. 5d, top; see Supplementary Fig. 13 for details), to assess the Kondo resonance. Coinciding with the observations of the Kondo effect, the SC gap size remains mostly unchanged, but the gap depth shows a dome-like evolution (Fig. 5d, bottom). The gap size is not suppressed by the local moment owing to the Kondo screening by the itinerant electrons when the Kondo temperature T_K is higher than the SC transition temperature T_c. The additional role of the Cr dopants is the electron doping, which may result in the dome-like evolution of the gap depth. The enhancement of the gap depth indicates a distinct superconductivity phase. Following the disappearance of the Kondo effect, both the gap size and depth suddenly drop when $x > 0.05$. As the Cr concentration increases further, suppression of both the superconductivity and Kondo effect is observed. In the doping range of $0.05 > x > 0.012$, despite the continuous increase of the Kondo resonance peak, the SC gap depth starts to decrease. Such behaviour may arise from additional effects introduced by Cr dopants beyond the formation of local moments, such as disorder-induced suppression of superconductivity[52] or band renormalization effects[53]. Once the doping exceeds a

certain level, these mechanisms may become more influential than local-moment physics, resulting in a reduction of the SC gap even as the Kondo signature grows.

Here, we show that dilute magnetic doping in a kagome superconductor generates spatially anisotropic Kondo resonances that locally break crystalline symmetries and couple strongly to the SC state. By linking frustrated magnetism to symmetry-breaking Kondo screening, our results point to a new route for manipulating superconductivity through local magnetic perturbations. More broadly, our work establishes an impurity engineering platform to tune the balance between Kondo screening, magnetic interactions and SC pairing. Extending this approach through controlled doping, pressure or heterostructure design may enable access to emergent regimes, including tunable Kondo lattices, quantum criticality and potentially topological SC phases.

Online content

Any methods, additional references, Nature Portfolio reporting summaries, source data, extended data, supplementary information, acknowledgements, peer review information; details of author contributions and competing interests; and statements of data and code availability are available at https://doi.org/10.1038/s41567-026-03292-6.

References

1. Stewart, G. R. Unconventional superconductivity. *Adv. Phys.* **66**, 75–196 (2017).
2. Scalapino, D. J. A common thread: the pairing interaction for unconventional superconductors. *Rev. Mod. Phys.* **84**, 1383–1417 (2012).
3. Ran, S. et al. Nearly ferromagnetic spin-triplet superconductivity. *Science* **365**, 684–687 (2019).
4. Ortiz, B. R. et al. New kagome prototype materials: discovery of KV_3Sb_5, RbV_3Sb_3, and CsV_3Sb_5. *Phys. Rev. Mater.* **3**, 094407 (2019).
5. Ortiz, B. R. et al. CsV_3Sb_5: a Z_2 topological kagome metal with a superconducting ground state. *Phys. Rev. Lett.* **125**, 247002 (2020).
6. Kang, M. et al. Twofold van Hove singularity and origin of charge order in topological kagome superconductor CsV_3Sb_5. *Nat. Phys.* **18**, 301–308 (2022).
7. Hu, Y. et al. Rich nature of van Hove singularities in Kagome superconductor CsV_3Sb_5. *Nat. Commun.* **13**, 2220 (2022).
8. Yang, S.-Y. et al. Giant, unconventional anomalous Hall effect in the metallic frustrated magnet candidate, KV_3Sb_5. *Sci. Adv.* **6**, eabb6003 (2020).
9. Chen, H. et al. Roton pair density wave in a strong-coupling kagome superconductor. *Nature* **599**, 222–228 (2021).
10. Deng, H. et al. Chiral kagome superconductivity modulations with residual Fermi arcs. *Nature* **632**, 775–781 (2024).
11. Han, X. et al. Atomic manipulation of the emergent quasi-2D superconductivity and pair density wave in a kagome metal. *Nat. Nanotechnol.* **20**, 1017–1025 (2025).
12. Nie, L. et al. Charge-density-wave-driven electronic nematicity in a kagome superconductor. *Nature* **604**, 59–64 (2022).
13. Wu, P. et al. Unidirectional electron–phonon coupling in the nematic state of a kagome superconductor. *Nat. Phys.* **19**, 1143–1149 (2023).
14. Li, H. et al. Unidirectional coherent quasiparticles in the high-temperature rotational symmetry broken phase of AV_3Sb_5 kagome superconductors. *Nat. Phys.* **19**, 637–643 (2023).
15. Xu, H.-S. et al. Multiband superconductivity with sign-preserving order parameter in kagome superconductor CsV_3Sb_5. *Phys. Rev. Lett.* **127**, 187004 (2021).
16. Hu, B. et al. Evidence of a distinct collective mode in Kagome superconductors. *Nat. Commun.* **15**, 6109 (2024).
17. Yu, F. H. et al. Unusual competition of superconductivity and charge-density-wave state in a compressed topological kagome metal. *Nat. Commun.* **12**, 3645 (2021).
18. Chen, K. Y. et al. Double superconducting dome and triple enhancement of T_c in the kagome superconductor CsV_3Sb_5 under high pressure. *Phys. Rev. Lett.* **126**, 247001 (2021).
19. Yang, H. et al. Titanium doped kagome superconductor $CsV_{3-x}TiSb_5$ and two distinct phases. *Sci. Bull.* **67**, 2176–2185 (2022).
20. Sur, Y., Kim, K.-T., Kim, S. & Kim, K. H. Optimized superconductivity in the vicinity of a nematic quantum critical point in the kagome superconductor $Cs(V_{1-x}Ti_x)_3Sb_5$. *Nat. Commun.* **14**, 3899 (2023).
21. Zhong, Y. et al. Nodeless electron pairing in CsV_3Sb_5-derived kagome superconductors. *Nature* **617**, 488–492 (2023).
22. Luo, Y. et al. A unique van Hove singularity in kagome superconductor $CsV_{3-x}Ta_xSb_5$ with enhanced superconductivity. *Nat. Commun.* **14**, 3819 (2023).
23. Ding, G., Wo, H., Gu, Y., Gu, Y. & Zhao, J. Effect of chromium doping on superconductivity and charge density wave order in the kagome metal $Cs(V_{1-x}Cr_x)_3Sb_5$. *Phys. Rev. B* **106**, 235151 (2022).
24. Yousuf, S. et al. Synthesis and physical properties of Cr-doped Kagome superconductor CsV_3Sb_5. *Curr. Appl. Phys.* **61**, 7–11 (2024).
25. Suzuki, S. et al. Evolution of band structure in the kagome superconductor $Cs(V_{1-x}Cr_x)_3Sb_5$: Toward universal understanding of charge density wave and superconducting phase diagrams. *Phys. Rev. B* **110**, 165104 (2024).
26. Liu, Y. et al. Superconductivity under pressure in a chromium-based kagome metal. *Nature* **632**, 1032–1037 (2024).
27. Li, Y. et al. Electron correlation and incipient flat bands in the Kagome superconductor $CsCr_3Sb_5$. *Nat. Commun.* **16**, 3229 (2025).
28. Zhao, H. et al. Cascade of correlated electron states in the kagome superconductor CsV_3Sb_5. *Nature* **599**, 216–221 (2021).
29. Kondo, J. Resistance minimum in dilute magnetic alloys. *Prog. Theor. Phys.* **32**, 37–49 (1964).
30. Ternes, M. Probing magnetic excitations and correlations in single and coupled spin systems with scanning tunneling spectroscopy. *Prog. Surf. Sci.* **92**, 83–115 (2017).
31. Zhang, Y. et al. Temperature and magnetic field dependence of a Kondo system in the weak coupling regime. *Nat. Commun.* **4**, 2110 (2013).
32. Madhavan, V., Chen, W., Jamneala, T., Crommie, M. F. & Wingreen, N. S. Local spectroscopy of a Kondo impurity: Co on Au(111). *Phys. Rev. B* **64**, 165412 (2001).
33. Knorr, N., Schneider, M. A., Diekhöner, L., Wahl, P. & Kern, K. Kondo effect of single co adatoms on cu surfaces. *Phys. Rev. Lett.* **88**, 096804 (2002).
34. Frota, H. O. & Oliveira, L. N. Photoemission spectroscopy for the spin-degenerate Anderson model. *Phys. Rev. B* **33**, 7871–7874 (1986).
35. Frota, H. O. Shape of the Kondo resonance. *Phys. Rev. B* **45**, 1096–1099 (1992).
36. Moore, J. E. & Wen, X.-G. Anomalous magnetic splitting of the kondo resonance. *Phys. Rev. Lett.* **85**, 1722–1725 (2000).
37. Costi, T. A. Kondo effect in a magnetic field and the magnetoresistivity of kondo alloys. *Phys. Rev. Lett.* **85**, 1504–1507 (2000).
38. Turco, E. et al. Demonstrating Kondo behavior by temperature-dependent scanning tunneling spectroscopy. *Phys. Rev. Res.* **6**, L022061 (2024).
39. Friedrich, F., Odobesko, A., Bouaziz, J., Lounis, S. & Bode, M. Evidence for spinarons in Co adatoms. *Nat. Phys.* **20**, 28–33 (2024).

40. Rubio-Verdú, C. et al. Orbital-selective spin excitation of a magnetic porphyrin. *Commun. Phys.* **1**, 15 (2018).
41. Schneider, M. A., Vitali, L., Knorr, N. & Kern, K. Observing the scattering phase shift of isolated Kondo impurities at surfaces. *Phys. Rev. B* **65**, 121406 (2002).
42. Kumar, N. et al. Atomic-scale magnetic doping of monolayer stanene by revealing Kondo effect from self-assembled Fe spin entities. *npj Quantum Mater.* **9**, 37 (2024).
43. Wang, Y. et al. Interplay of nanoscale strain and smectic susceptibility in kagome superconductors. *Phys. Rev. X* **15**, 021074 (2025).
44. Wang, Z. et al. Electronic nature of chiral charge order in the kagome superconductor CsV_3Sb_5. *Phys. Rev. B* **104**, 075148 (2021).
45. Boucaï, E., Lecoanet, B., Pilon, J., Tholence, J. L. & Tournier, R. Interaction effects between nearly magnetic cobalt impurities in gold. *Phys. Rev. B* **3**, 3834–3846 (1971).
46. Song, B. et al. Realization of Kagome Kondo lattice. *Nat. Commun.* **16**, 5643 (2025).
47. Ruan, W. et al. Visualization of the periodic modulation of Cooper pairing in a cuprate superconductor. *Nat. Phys.* **14**, 1178–1182 (2018).
48. Xu, J.-P. et al. Experimental detection of a Majorana mode in the core of a magnetic vortex inside a topological insulator-superconductor $Bi_2Te_3/NbSe_2$ heterostructure. *Phys. Rev. Lett.* **114**, 017001 (2015).
49. Yuan, Y. et al. Evidence of anisotropic Majorana bound states in 2M-WS_2. *Nat. Phys.* **15**, 1046–1051 (2019).
50. Kong, L. et al. Half-integer level shift of vortex bound states in an iron-based superconductor. *Nat. Phys.* **15**, 1181–1187 (2019).
51. Huang, Z. et al. Tunable vortex bound states in multiband CsV_3Sb_5-derived kagome superconductors. *Sci. Bull.* **69**, 885–892 (2024).
52. Li, B. Chemical doping effect in the $LaRu_3Si_2$ superconductor with a kagome lattice. *Phys. Rev. B* **94**, 094523 (2016).
53. Peng, S. et al. Flat bands and distinct density wave orders in correlated Kagome superconductor $CsCr_3Sb_5$. *Sci. China Phys. Mech. Astron.* **69**, 217412 (2025).

Methods

Single crystal growth of $CsV_{3-x}Cr_xSb_5$

Single crystals of $CsV_{3-x}Cr_xSb_5$ were grown via a modified self-flux method[12,20].

STM/STS

The samples used in the STM/STS experiments were cleaved at low temperature (10 K) and immediately transferred to an STM chamber and cooled down to 4.2 K. Experiments were performed in an ultrahigh vacuum (1×10^{-10} mbar) ultralow temperature STM system equipped with an external magnetic field perpendicular to the sample surface. The lowest base temperature is 5 mK, with an electronic temperature of 138 mK (calibrated using a standard superconductor, Al crystal). The magnetic field was applied using the zero-field cooling technique. All the scanning parameters (setpoint voltage V_s and tunnelling current I_t) of the STM topographic images are listed in the figure captions. The dI/dV spectra were acquired by a standard lock-in amplifier at a modulation frequency of 973.1 Hz, and the modulation bias (V_{mod}) is listed in the figure captions. Non-magnetic tungsten tips were fabricated via electrochemical etching and calibrated on a clean Au(111) surface prepared by repeated cycles of sputtering with argon ions and annealing at 500 °C.

Identification of Cr concentrations

The diluted Cr concentrations were determined microscopically by counting numbers of dumbbell-like protrusions with high accuracy in STM images of Sb-terminated surfaces (Fig. 1b–d). With the Cr concentration further increasing to $x > 0.054$, it becomes difficult to discern the number of dumbbell-like protrusions in STM images (Fig. 1e–g), so the concentrations were verified macroscopically by energy-dispersive x-ray spectroscopy.

DFT calculations

The DFT calculations were carried out using the generalized gradient approximation for the exchange–correlation potential in the Perdew–Burke–Ernzerhof (PBE) form[54] with the projector augmented wave method[55] and a plane-wave basis set as implemented in the Vienna ab initio simulation package (VASP)[56]. We also included the dispersion correction through Grimme's semiempirical D3 scheme[57] in combination with the PBE functional (PBE-D3). A kinetic energy cut-off of 350 eV for the planewave basis was adopted for structural relaxations and electronic structure calculations. A $6 \times 6 \times 2$ asymmetric slab model was used in our calculations. A vacuum layer of 20 Å in thickness was used to reduce imaging interactions between adjacent supercells. Dipole correction was considered in all calculations to correct the error introduced by the periodic boundary condition and balance the vacuum level differences on the different sides of polarized surfaces[58]. The lowest layer of the CsV_3Sb_5 slab was fixed, whereas the remaining layers were allowed to relax until the residual force per atom was below 0.01 eV Å^{-1}. In the topmost layer, one vanadium (V) atom was replaced by a chromium (Cr) atom to model the substitution of V by Cr. A gamma-only $\mathbf{k}$-mesh was used to sample the Brillouin zone of the super cell. The Methfessel–Paxton method with a σ value of 0.05 eV was applied for structural relaxation and electronic structure calculations. The STM images were calculated using the Tersoff–Hamann method[59].

Data availability

The data supporting the findings of this study are available via the Science Data Bank at https://doi.org/10.57760/sciencedb.32867. Additional data are available from the corresponding authors upon reasonable request. Source data are provided with this paper.

Code availability

The code used for STM data analysis is available from the corresponding authors upon reasonable request.

References

54. Perdew, J. P., Burke, K. & Ernzerhof, M. Generalized gradient approximation made simple. *Phys. Rev. Lett.* **77**, 3865–3868 (1996).
55. Blöchl, P. E. Projector augmented-wave method. *Phys. Rev. B* **50**, 17953–17979 (1994).
56. Kresse, G. & Furthmüller, J. Efficient iterative schemes for ab initio total-energy calculations using a plane-wave basis set. *Phys. Rev. B* **54**, 11169–11186 (1996).
57. Grimme, S., Antony, J., Ehrlich, S. & Krieg, H. A consistent and accurate ab initio parametrization of density functional dispersion correction (DFT-D) for the 94 elements H-Pu. *J. Chem. Phys.* **132**, 154104 (2010).
58. Neugebauer, J. & Scheffler, M. Adsorbate-substrate and adsorbate-adsorbate interactions of Na and K adlayers on Al(111). *Phys. Rev. B* **46**, 16067–16080 (1992).
59. Tersoff, J. & Hamann, D. R. Theory and application for the scanning tunneling microscope. *Phys. Rev. Lett.* **50**, 1998–2001 (1983).

Acknowledgements

We thank Z. Wang for helpful discussions. The work is supported by grants from the National Natural Science Foundation of China (grant nos. 62488201 to H.-J.G., 92580202 to H.C., 92477205 to W.J. and 52461160327 to W.J.), the National Key Research and Development Projects of China (grant nos. 2022YFA1204100 to H.Y. and H.C. and 2023YFA1406500 to W.J.), the CAS Project for Young Scientists in Basic Research (grant no. YSBR-003 to H.C.) and the Innovation Program of Quantum Science and Technology (grant no. 2021ZD0302700 to H.-J.G., H.C. and H.Y.). Z.W. is supported by the US DOE, Basic Energy Sciences (grant no. DE-FG02-99ER45747) and by Research Corporation for Science Advancement (Cottrell SEED award no. 27856). Calculations (W.J.) were performed at the Physics Lab of High-Performance Computing (PLHPC) and the Public Computing Cloud (PCC) of Renmin University of China.

Author contributions

H.-J.G. and H.C. designed the experiments. Z.H., H.C. and H.Z. performed the STM/STS experiments and data analysis. Z. Zhao, R.W. and H.Y. prepared the Cr-doped CsV_3Sb_5 samples. Z.W. did the theoretical consideration. Z. Zhang and W.J. carried out the theoretical calculations and analysis. Z.H., H.C., Z. Zhang, W.J. and H.-J.G. wrote the paper with input from all authors. H.-J.G. supervised the project.

Competing interests

The authors declare no competing interests.

Additional information

Supplementary information The online version contains supplementary material available at https://doi.org/10.1038/s41567-026-03292-6.

Correspondence and requests for materials should be addressed to Hui Chen, Wei Ji or Hong-Jun Gao.

Peer review information *Nature Physics* thanks the anonymous reviewer(s) for their contribution to the peer review of this work.